Turbulent/non-turbulent interfaces detected in DNS of incompressible turbulent boundary layers

T. Watanabe, X. Zhang, and K. Nagata

Citation: Physics of Fluids **30**, 035102 (2018); doi: 10.1063/1.5022423
View online: https://doi.org/10.1063/1.5022423
View Table of Contents: http://aip.scitation.org/toc/phf/30/3
Published by the American Institute of Physics

Turbulent/non-turbulent interfaces detected in DNS of incompressible turbulent boundary layers

T. Watanabe,[a] X. Zhang, and K. Nagata
Department of Aerospace Engineering, Nagoya University, Nagoya, Japan

(Received 15 January 2018; accepted 14 February 2018; published online 5 March 2018)

The turbulent/non-turbulent interface (TNTI) detected in direct numerical simulations is studied for incompressible, temporally developing turbulent boundary layers at momentum thickness Reynolds number $Re_\theta \approx 2000$. The outer edge of the TNTI layer is detected as an isosurface of the vorticity magnitude with the threshold determined with the dependence of the turbulent volume on a threshold level. The spanwise vorticity magnitude and passive scalar are shown to be good markers of turbulent fluids, where the conditional statistics on a distance from the outer edge of the TNTI layer are almost identical to the ones obtained with the vorticity magnitude. Significant differences are observed for the conditional statistics between the TNTI detected by the kinetic energy and vorticity magnitude. A widely used grid setting determined solely from the wall unit results in an insufficient resolution in a streamwise direction in the outer region, whose influence is found for the geometry of the TNTI and vorticity jump across the TNTI layer. The present results suggest that the grid spacing should be similar for the streamwise and spanwise directions. Comparison of the TNTI layer among different flows requires appropriate normalization of the conditional statistics. Reference quantities of the turbulence near the TNTI layer are obtained with the average of turbulent fluids in the intermittent region. The conditional statistics normalized by the reference turbulence characteristics show good quantitative agreement for the turbulent boundary layer and planar jet when they are plotted against the distance from the outer edge of the TNTI layer divided by the Kolmogorov scale defined for turbulent fluids in the intermittent region. *Published by AIP Publishing.* https://doi.org/10.1063/1.5022423

I. INTRODUCTION

Turbulent boundary layers can be seen in a wide range of problems. In engineering applications, they are related to skin friction, heat and mass transfer, and aerodynamic performance of airfoils, wings, and wind turbines. They are also important in meteorology since atmospheric boundary layers develop over land and sea surfaces affecting dispersion of pollutants and profiles of wind speed, temperature, and moisture. The importance of boundary layers has been recognized over a century, and a large number of research papers have been devoted to understand turbulent boundary layers from many aspects, e.g., similarity laws of velocity statistics,[1–3] coherent structures,[4–6] Reynolds number effects,[7–9] and multiscale processes in the logarithmic layer,[10] and the effect of wall roughness.[11]

An outermost part of turbulent boundary layers is highly intermittent, where a contorted interface separates turbulence from non-turbulent fluids in freestream.[12] The nature of the intermittent region has been revealed with conditional sampling methods with hot-wire anemometry.[13] For example, it was found that a vertical profile of intermittency factor, a probability that a flow at a given point is turbulent, is approximated by an error function;[14,15] motions of turbulent and non-turbulent fluids in the outer region are related to large-scale structures in turbulent boundary layers such as a turbulent bulge.[16] The contorted interface has also been found in free shear flows (e.g., jets, mixing layers, and wakes), to which the same conditional sampling methods have been applied.[17–19]

The interface separating turbulent from non-turbulent fluids is called the turbulent/non-turbulent interface (TNTI). The properties of the TNTI have been revealed in recent studies based on direct numerical simulations (DNSs) and high-resolution three- or two-dimensional measurements as summarized in a review paper.[20] Most of these studies rely on conditional statistics computed as a function of a distance from the TNTI.[21] The vorticity level is matched between turbulent-core and non-turbulent regions in a layer with a finite thickness, which is referred to as a TNTI layer. The TNTI layer can be divided into two layers based on vorticity dynamics:[22,23] one is called a viscous superlayer, where a fluid acquires vorticity by viscous diffusion and the other one is called a turbulent sublayer[20] (or buffer layer[23]), where inviscid vortex stretching is as important as viscous effects. In unbounded turbulent flows, the relationship between entrainment processes and the TNTI layer is also investigated with both Eulerian and Lagrangian statistics.[24–30]

The TNTI layer in turbulent boundary layers is also studied as well as in unbounded flows. The conditional statistics near the TNTI layer are reported based on the DNS of turbulent boundary layers,[31] where the TNTI layer was shown to act as a barrier to irrotational velocity fluctuations in freestream in consistency with the blocking mechanism.[32] Borrel and Jiménez also used the DNS and extensively studied the geometry of the TNTI layer for a wide range of threshold in the detection of the TNTI.[33] The effects of large-scale motions in turbulent

[a]watanabe.tomoaki@c.nagoya-u.jp

boundary layers on the TNTI are also reported by Lee *et al.*,[34] where the characteristics of the TNTI, such as a shape of the TNTI and spatial variation of the interface height, are explained with the large-scale structures underneath the TNTI. Experiments with particle image velocimetry (PIV) have revealed the flow properties near the TNTI layer in turbulent boundary layers at a higher Reynolds number than in the DNS.[35–37]

These DNS studies of the TNTI layer in turbulent boundary layers considered spatially developing boundary layers, where the boundary layer develops in the streamwise direction. Recently, Kozul *et al.*[38] have examined temporal simulations of turbulent boundary layers, where the boundary layer grows with time in a computational domain which is periodic in the streamwise direction. They have shown that the temporal boundary layer is a good model for the spatial counterpart in a fully developed state. Similar temporal simulations have been used to provide a model of spatially developing free shear flows.[39,40] One of the advantages in the temporal simulations is a low computational cost: Kozul *et al.*[38] showed that the number of the computational grid points required in spatial simulations is about 30 times larger than in temporal simulations for turbulent boundary layers at the same Reynolds number. The TNTI layers in free shear flows have often been studied with temporal simulations.[23,39,41–43]

In the present study, the TNTI layer is investigated in temporally developing boundary layers with DNSs. The DNS results are analyzed for addressing following issues: (a) a detector function of the TNTI, (b) spatial resolutions required for studying the TNTI in turbulent boundary layers, and (c) statistical properties of turbulence characterizing the TNTI layer. Regarding (a), previous studies on the TNTI layers in turbulent boundary layers have used various quantities for detecting the TNTI although the essential characteristic of the turbulence is vorticity.[14] This is because it is difficult to measure all components of the vorticity vector. A passive scalar has been widely used as a marker of turbulent fluids.[44] Spanwise vorticity and (turbulent) local kinetic energy are also used in recent experimental studies on the TNTI in turbulent boundary layers.[36,45] So far, the influence of detector functions is not well known for the conditional statistics used for studying the local structure of the TNTI layer in turbulent boundary layers even though various detector functions result in a similar profile of intermittency factor.[34,36,46] The requirement of the spatial resolution is also unclear for the TNTI in the boundary layer. The number of the grid points in the DNS of wall-bounded flows is usually determined based on the viscous length ν/u_τ,[47] where u_τ is the friction velocity and ν is the kinematic viscosity, although the structures of the turbulence are different between the near-wall region and the intermittent region. This study examines the influence of the spatial resolution on the geometry of the TNTI and the conditional statistics. The turbulence characteristic related to the TNTI layer is also considered because the conditional statistics of the TNTI layer must be normalized by appropriate quantities in order to compare different flows. The statistics of turbulent fluids in the intermittent region are introduced because the TNTI layer is formed around the turbulent fluids in this region. It is shown that the conditional statistics normalized with the statistical properties of turbulence in the intermittent region are quantitatively similar for a turbulent boundary layer and a planar jet. These comparisons can be important to understand the TNTI layer in a wall jet.[48–50]

The DNS of the temporally developing boundary layers is described in Sec. II. Section III presents comparison of the present DNS with spatially developing boundary layers and the results related to the TNTI layer. Finally, Sec. IV summarizes the conclusions.

II. DNS OF TEMPORALLY DEVELOPING TURBULENT BOUNDARY LAYER

A. Temporally developing turbulent boundary layer

The DNS is performed for incompressible temporally developing boundary layers with passive scalar transfer.[38] Governing equations are Navier-Stokes equations and advective-diffusion equations for passive scalar ϕ, which are written as

$$\frac{\partial u_j}{\partial x_j} = 0, \tag{1}$$

$$\frac{\partial u_i}{\partial t} + \frac{\partial u_i u_j}{\partial x_j} = -\frac{\partial p}{\partial x_i} + \nu \frac{\partial^2 u_i}{\partial x_j \partial x_j}, \tag{2}$$

$$\frac{\partial \phi}{\partial t} + \frac{\partial u_j \phi}{\partial x_j} = D_\phi \frac{\partial^2 \phi}{\partial x_j \partial x_j}, \tag{3}$$

where x_i, t, u_i, p, and D_ϕ denote the position, time, velocity, pressure divided by a constant density ρ, and molecular diffusivity coefficient of ϕ, respectively. The boundary layer develops with time in a computational domain with periodic boundary conditions in the streamwise and spanwise directions. Thus, the flow does not grow in the streamwise direction but develops with time. Figure 1 shows a schematic of

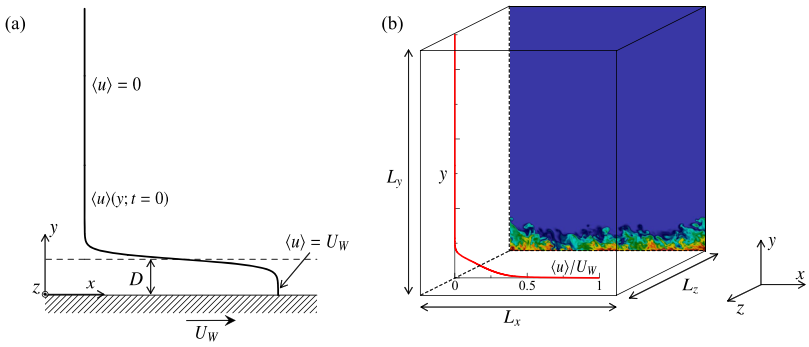

FIG. 1. Schematic diagram of the DNS of temporally developing boundary layers: (a) initial velocity profile and (b) computational domain with the mean velocity profile (red line) and instantaneous scalar field on the x-y plane (color contour) in a fully developed state.

the temporally developing boundary layer. The DNS is based on the reference frame where the wall is moving at a constant speed U_W while a fluid far from the wall is quiescent. x, y, and z denote the streamwise, wall-normal, and spanwise directions, respectively, and the velocity components in these directions are u, v, and w. An instantaneous value of physical variables $f(x, y, z; t)$ can be decomposed into mean and fluctuating components $f(x, y, z; t) = \langle f\rangle(y; t) + f'(x, y, z; t)$ based on an averaging procedure $\langle\ \rangle$ in two periodic directions. The flow is initialized with the mean velocity profile that approximates the flow induced by a trip-wire on the wall given by[38]

$$\langle u\rangle(y; t = 0) = \frac{1}{2}U_W + \frac{1}{2}U_W \tanh\left[\frac{D}{2\theta_S}\left(1 - \frac{y}{D}\right)\right], \quad (4)$$

$$\langle v\rangle(y; t = 0) = \langle w\rangle(y; t = 0) = 0, \quad (5)$$

and fluctuating components u', v', and w', where D is the diameter of the trip-wire and $\theta_S = 0.1D$ is the initial shear layer thickness. The fluctuating components are non-zero only in the near wall region of $y < D$, where they are generated by a diffusion process that produces spatially correlated noise.[51] The conditions of the simulation can be determined by specifying non-dimensional numbers: the trip-wire Reynolds number $Re_D = U_W D/\nu$ and the Schmidt number $Sc = \nu/D_\phi$. The influence of Re_D has been studied in detail by Kozul *et al.*:[38] Re_D must exceed a critical value (~500) for simulating turbulent boundary layers; as the momentum thickness $\theta(t)$ approaches D with time, the flow becomes independent of Re_D, where $\theta(t) = \int_0^\infty \langle u\rangle(U_W - \langle u\rangle)/U_W^2 \mathrm{d}y$. The simulations are designed for investigating turbulent boundary layers at the Reynolds number based on the momentum thickness, $Re_\theta = U_W\theta/\nu$, up to 2100. Then, $Re_D = 2000$ is used in the DNS so that $\theta \approx D$ when the flow reaches $Re_\theta \approx 2000$. The same value of $Re_D = 2000$ was also used in the previous DNS of temporally developing boundary layers.[38] For the passive scalar ϕ, $Sc = 1$ in all simulations, and the initial profile is given by

$$\phi = \frac{1}{2}\phi_W + \frac{1}{2}\phi_W \tanh\left[\frac{D}{2\theta_S}\left(1 - \frac{y}{D}\right)\right], \quad (6)$$

where ϕ_W is a constant value of ϕ on the wall.

The next step for setting up the simulations is choosing the size of the computational domain ($L_x \times L_y \times L_z$) in relation to D. The domain must be larger than the length of the largest structure in the flow, which can be estimated by 99% boundary layer thickness δ_{99} defined as the vertical location where $(U_W - \langle u\rangle)/U_W = 0.99$. Following previous studies,[38,52,53] $L_x > 2\pi\delta_{99}$, $L_y > 3\delta_{99}$, and $L_z > \pi\delta_{99}$ are ensured at the final step of the simulations. δ_{99} in the fully developed region can be estimated as $\delta_{99} \approx 8\theta$ from the previous DNS of turbulent boundary layers.[38] Then, $\delta_{99} \approx (8Re_\theta/Re_D)D$ is used for estimating δ_{99}/D for Re_θ at the end of the simulations. For $Re_D = 2000$ and $Re_\theta = 2100$, the conditions of $L_x > 2\pi\delta_{99}$, $L_y > 3\delta_{99}$, and $L_y > \pi\delta_{99}$ are satisfied for $L_x > 52.8D$, $L_y > 25.2D$, and $L_z > 26.4D$. The computational domain with $(L_x, L_y, L_z) = (56D, 70D, 28D)$ is used based on these estimations of the required domain size. $L_y = 70D$ is chosen so that the grid spacing is appropriate near the wall and in the intermittent region by testing various values for three parameters: the vertical domain size L_y, the number of grid points in the vertical direction, and a parameter of a mapping function used for setting the vertical coordinate given below.

The simulations are performed with a DNS code based on a finite difference method. The computational domain is represented by ($N_x \times N_y \times N_z$) grid points. Uniform grid spacing is used in the homogeneous directions while the vertical location y of the grid is given with an integer $j = 1, \ldots, N_y$ using the mapping function that gives smaller grid size near the wall,

$$y(j) = L_y\left[1 - \frac{1}{\tanh\alpha_y}\tanh\left(\alpha_y\left(1 - \frac{j-1}{N_y - 1}\right)\right)\right] \quad (7)$$

with $\alpha_y = 3$. The number of the grid points should be large enough for the DNS to resolve the smallest scales of the flow. In the DNS of wall-bounded flows, the grid spacing is often determined based on the viscous length ν/u_τ, where $u_\tau = \sqrt{\tau_w/\rho}$ is the friction velocity and $\tau_w = -\rho\nu(\partial\langle u\rangle/\partial y)_W$ is the wall shear stress (subscript W refers a value on the wall). The number of the grid points is often determined so that $\Delta_x^+ < 9.7, \Delta_{yW}^+ < 0.2$, and $\Delta_z^+ < 4.8$, where Δ_{yW}^+ is the vertical grid spacing of the grid point closest to the wall and $\Delta_i^+ = \Delta_i/(\nu/u_\tau)$ is the grid spacing in a dimensionless wall unit.[38,47,52,54] A larger grid spacing in the x direction is related to alternating high and low speed streaks elongated in the streamwise direction near the wall. The characteristics of turbulence, such as length scales and structures, significantly vary in the wall normal direction in the boundary layer. The outer region contains three-dimensional small-scale vortical structures.[55] In this region, the grid spacing should be determined based on the Kolmogorov length scale of turbulence as in numerical simulations of unbounded turbulent flows. Here, the smallest scale that characterizes turbulence should be carefully determined when the intermittent region is of interest because the non-turbulent region has much larger Kolmogorov length scale than the turbulent region.[56] The DNS of the turbulent boundary layers is performed with a coarse grid (CG), fine grid (FG), and very fine grid (VFG) as summarized in Table I. It should be noted that the grid spacing in the CG is small enough to satisfy the criteria based on the viscous length ν/u_τ but still relatively coarse compared with the FG and VFG. The number of the grid points in the FG and VFG is determined based on the Kolmogorov scale in the outer region as discussed in Sec. III.

B. Numerical methods

The governing equations are solved on a staggered grid with the DNS code based on a fractional step method with fully conservative finite-difference schemes[57] for spatial discretization and a third-order Runge-Kutta method for temporal advancement. The message passing interface (MPI) is used for parallelizing the DNS code employing a 2D pencil

TABLE I. DNS of temporally developing turbulent boundary layers. Δ_i^+ is taken from boundary layers at $Re_\theta = 2100$.

Case	Re_θ	N_x	N_y	N_z	Δ_x^+	Δ_{yW}^+	Δ_z^+
CG	2100	576	861	576	8.2	0.20	4.1
FG	2100	1152	1001	576	4.8	0.19	4.8
VFG	2100	1536	1001	768	3.0	0.19	3.0

decomposition applied with an x-pencil orientation. The same code has been used with different initial and boundary conditions in our previous studies.[58–60] The DNS code is based on the fourth-order fully conservative central difference scheme for the homogeneous directions and the second-order fully conservative central difference scheme for the wall normal direction. These fourth- and second-order schemes are widely used in the DNS of channel flows.[61–64] The Poisson equation for pressure is solved with the biconjugate gradient stabilized (BiCGStab) method. Variables are stored in a staggered grid arrangement. The wall is treated with non-slip boundary conditions while the top of the computational domain is a slip wall. The periodic boundary conditions are applied in the homogeneous directions.

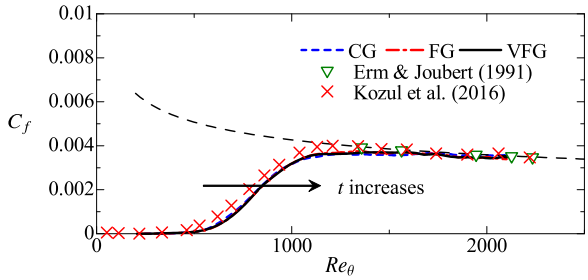

FIG. 3. Temporal variations of skin friction coefficient C_f as a function of momentum thickness Reynolds number Re_θ. The present DNS is compared with experiments of the spatially developing boundary layer[65] and DNS of the temporally developing boundary layer.[38] The thin broken line represents a friction law of turbulent boundary layers $C_f = 0.0024Re_\theta^{-1/4}$.

III. RESULTS AND DISCUSSION

A. Comparison with experiments and DNS of spatially developing boundary layers

Figure 2 visualizes passive scalar on an x-y plane at different time steps. The turbulent boundary layer develops with time as attested from the temporal growth of the boundary layer thickness. The present DNS is validated by comparing the statistics with experiments and DNS of spatially developing boundary layers with similar Re_θ. Figure 3 shows the variation of the skin friction coefficient $C_f = \tau_w/(\rho U_W^2/2)$ against Re_θ in comparison with a friction law of turbulent boundary layers[67] $C_f = 0.0024Re_\theta^{-1/4}$, DNS of temporally developing boundary layers,[38] and experiments.[65] In the temporal simulations, Re_θ increases with time. The temporal variation of (C_f, Re_θ) in the present DNS is similar to the previous study:[38] C_f and Re_θ increase with time from the initial state, and (C_f, Re_θ) follows the friction law after the boundary layer has developed in agreement with the experiments.

Figure 4 compares vertical profiles of mean velocity and rms velocity fluctuations normalized by the friction velocity and viscous length. Here, $U^+ = (U_W - \langle u\rangle)/u_\tau$, $u^+ = \sqrt{\langle u^2\rangle - \langle u\rangle^2}/u_\tau$, and $v^+ = \sqrt{\langle v^2\rangle - \langle v\rangle^2}/u_\tau$ while $y^+ = y/(\nu/u_\tau)$. The present results are compared with DNS and experiments of spatially developing boundary layers.[65,66] The mean velocity profile is also compared with $U^+ = y^+$ and $U^+ = (1/\kappa)\ln y^+ + A$ ($\kappa = 0.41$ and $A = 5.1$), which are expected to hold in the viscous sublayer and log-low region, respectively. The present results agree well with these relations and with previous DNS and experiments for all grid settings in Table I.

B. Detection of the outer edge of turbulent/non-turbulent interface layer

Hereafter, statistics at $y/\delta_{99} = 0.5$ are used as reference quantities for two reasons: this location is far from the wall, where U^+ does not follow the log-law in Fig. 4(a); non-turbulent fluids hardly reach $y/\delta_{99} = 0.5$ and the statistics at this location are computed from turbulent fluids without including the contribution of non-turbulent fluids. The quantities evaluated at $y/\delta_{99} = 0.5$ are represented with subscript r. Figure 5

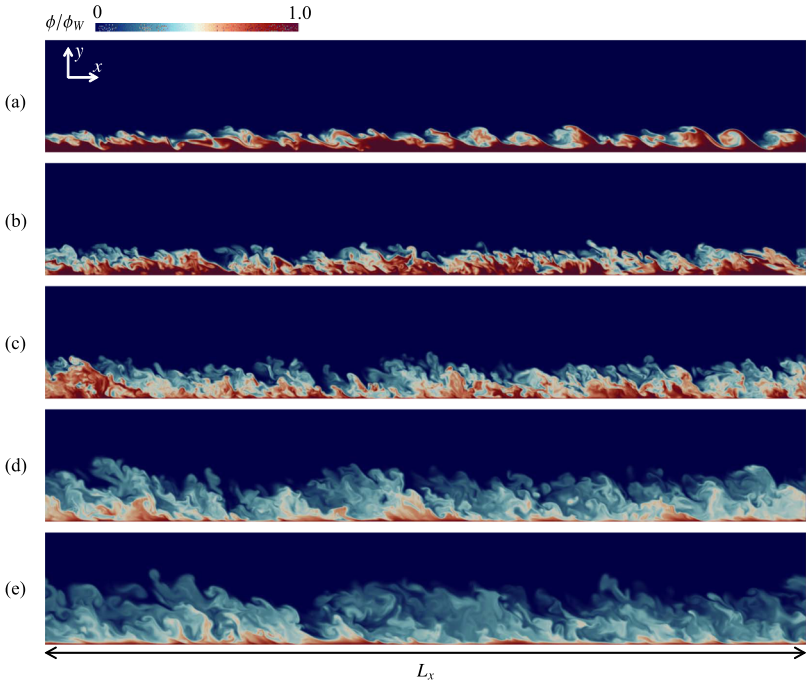

FIG. 2. Temporal development of the turbulent boundary layer. Passive scalar ϕ on the x-y plane is visualized at (a) $t = 15.8(D/U_W)$ ($Re_\theta = 487$), (b) $t = 22.5(D/U_W)$ ($Re_\theta = 738$), (c) $t = 34.0(D/U_W)$ ($Re_\theta = 1023$), (d) $t = 59.6(D/U_W)$ ($Re_\theta = 1305$), and (e) $t = 88.1(D/U_W)$ ($Re_\theta = 1487$) in the FG.

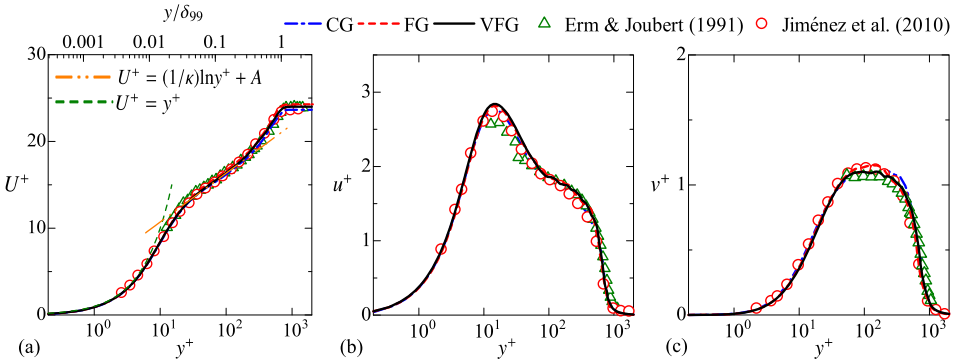

FIG. 4. Vertical profiles of (a) mean velocity, (b) rms streamwise velocity fluctuation, and (c) rms vertical velocity fluctuation at $Re_\theta = 2100$ in comparison with experiments[65] ($Re_\theta = 2260$) and DNS of spatially developing boundary layers[66] ($Re_\theta = 1986$).

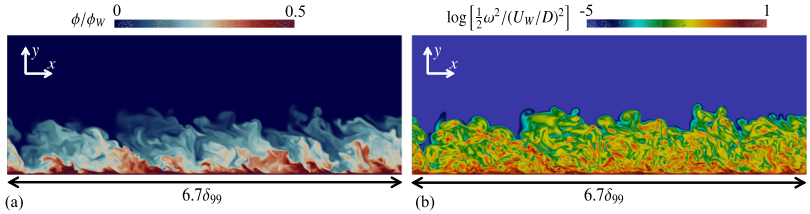

FIG. 5. Flow visualization with (a) passive scalar ϕ and (b) enstrophy $\omega^2/2$ on the x-y plane in the FG ($Re_\theta = 2100$).

visualizes the passive scalar ϕ and enstrophy $\omega^2/2 = \omega_i\omega_i/2$ field on an x-y plane, where ω_i is the vorticity vector. These quantities have been widely used as a marker of turbulent fluids in previous studies of intermittent flows.[13,20] Overall distributions of ϕ and $\omega^2/2$ are similar in Fig. 5. It is also found that the structures of strong vorticity regions change with the distance from the wall in Fig. 5 as mentioned in the Introduction.

The turbulent regions can be detected with vorticity magnitude $\omega = \sqrt{\omega_i\omega_i}$ following Corrsin and Kistler.[14] Thus, a fluid with $\omega \geq \omega_{th}$ can be defined as turbulent with an appropriate choice of the threshold ω_{th}. Then, the isosurface of $\omega = \omega_{th}$ is an infinitely thin surface separating turbulent from non-turbulent fluids. Detailed investigations of the TNTI layer require us to identify the location of $\omega = \omega_{th}$ within the TNTI layer. Here, the isosurface $\omega = \omega_{th}$ is assumed to be located at the outer edge of the TNTI layer: this isosurface is bounded to irrotational fluids and referred to as irrotational boundary following previous studies.[43] Then, the TNTI layer can be identified just inside the irrotational boundary.

The irrotational boundary is detected by choosing ω_{th} with the following method. Figure 6(a) shows the probability density function (PDF) of $\log_{10}\hat{\omega}$ ($\hat{\omega} = \omega/\langle\omega\rangle_r$) denoted by $P(\log_{10}\hat{\omega}; y)$ following Lee *et al.*[34] The vorticity level significantly varies in the wall-normal direction for $y/\delta_{99} > 0.5$. The threshold ω_{th} should be smaller than the minimum value of ω observed around $y/\delta_{99} \approx 0.25$ because these small values of ω near the wall are related to a weak vorticity region of turbulence.[68] Ambient fluids can possess very small vorticity because of numerical or measurement errors and background turbulence inhibited in wind tunnels in experiments. These fluids with small vorticity, which is not related to turbulent boundary layers, should be treated as non-turbulent fluids for studying the TNTI. This can be done by choosing the threshold from the vorticity level for which the isoline of the PDF for $y/\delta_{99} > 1$ is parallel to the abscissa in Fig. 6(a). These criteria roughly determine highest and lowest values of ω_{th} for detecting the irrotational boundary as shown in the vertical broken lines in Fig. 6(a). An actual value of ω_{th} is determined based on a volume of turbulent fluids, V_T, following previous studies.[28] The normalized turbulent volume $\hat{V}_T = V_T/L_xL_z\delta_{99}$ is plotted against $\log_{10}\hat{\omega}_{th}$ as shown in Fig. 6(b). $\hat{V}_T$ is related to the PDF of $\log_{10}\hat{\omega}$ by

$$\hat{V}_T = \frac{1}{\delta_{99}}\int_{\log_{10}\hat{\omega}_{th}}^{\infty}\int_0^{Ly} P(\log_{10}\hat{\omega}; y)\mathrm{d}y\mathrm{d}(\log_{10}\hat{\omega}). \quad (8)$$

There is a certain range of threshold for which $\hat{V}_T$ hardly changes with $\log_{10}\hat{\omega}_{th}$. Figure 6(b) also shows $-\mathrm{d}\hat{V}_T/\mathrm{d}\log_{10}\hat{\omega}_{th}$. The value of $\log_{10}\hat{\omega}_{th}$ for a minimum value of $-\mathrm{d}\hat{V}_T/\mathrm{d}\log_{10}\hat{\omega}_{th}$ gives the threshold for which the location of the isosurface $\omega = \omega_{th}$ is least sensitive to the threshold level $\log_{10}\hat{\omega}_{th}$. This threshold value satisfies $\mathrm{d}^2\hat{V}_T/\mathrm{d}(\log_{10}\hat{\omega}_{th})^2 = 0$

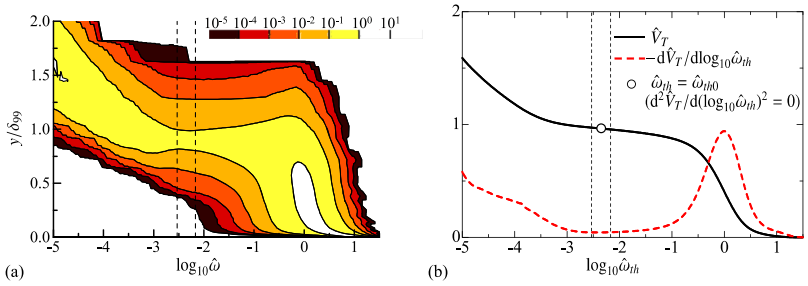

FIG. 6. (a) Vertical distribution of the PDF of normalized vorticity magnitude $\log_{10}\hat{\omega} = \log_{10}(\omega/\omega_r)$ ($\omega_r = \langle\omega\rangle$ at $y/\delta_{99} = 0.5$). (b) Volume of turbulent fluids with $\omega \geq \omega_{th}$ as a function of ω_{th}. Turbulent volume V_T is normalized by $L_xL_z\delta_{99}$ ($\hat{V}_T = V_T/L_xL_z\delta_{99}$). Results are taken from the FG at $Re_\theta = 2000$.

and is denoted by ω_{th0} shown as a circle in Fig. 6(b). ω_{th0} is located between the highest and lowest candidates of ω_{th} determined from the PDF of $\log_{10}\hat{\omega}_{th}$. The influence of the choice of ω_{th} is further examined between two vertical broken lines in Fig. 6 with statistics conditioned on a distance from the irrotational boundary in Subsection III C.

C. Procedure for computing statistics on interface coordinate

Statistics are computed conditioned on a distance from the irrotational boundary defined as the isosurface of $\omega = \omega_{th0}$. An interface coordinate ζ_I is taken for each point of $\omega = \omega_{th0}$, where the direction of the coordinate is given by a normal direction of the irrotational boundary given by $\mathbf{n} = -\nabla\omega/|\nabla\omega|$ as shown in Fig. 7 ($\mathbf{n}$ is shown on a two-dimensional plane for explanation in the figure although $\mathbf{n}$ is a three-dimensional vector). $\zeta_I = 0$ denotes the irrotational boundary while turbulent fluids are located for $\zeta_I < 0$. The interface coordinate is locally normal to the irrotational boundary for investigating the local structure of the TNTI layer unlike previous studies on turbulent boundary layers,[31] where the vertical distance from the TNTI is considered. The interface coordinate is defined for $-95\eta_r \le \zeta_I \le 95\eta_r$, where ζ_I is discretized by 360 points and η_r is the Kolmogorov scale at $y/\delta_{99} = 0.5$. Flow variables, such as velocity and vorticity magnitude, are interpolated onto the discretized points of the interface coordinate from the computational grid of the DNS with the tri-linear interpolation scheme. Then, the conditional statistics are computed as a function of ζ_I in each snapshot. The interface coordinate might cross more than one irrotational boundary point although the statistics need to be computed separately for turbulent and non-turbulent fluids. Some parts of the interface coordinate are excluded from the analysis as shown with broken lines in Fig. 7. All fluids on the interface coordinate are excluded from the analysis when the local coordinate crosses another irrotational boundary at $|\zeta_I| < \Delta_\zeta$ as shown by the broken line of (a) in Fig. 7, where Δ_ζ is determined below. The region within a distance of Δ_ζ from another irrotational boundary on the interface coordinate is also excluded from the statistical analysis, whose example is shown by the broken lines of (b) in Fig. 7. The conditional statistics are examined by changing Δ_ζ from $5\eta_r$ to $25\eta_r$. Hereafter, the conditional average is denoted by $\langle\ \rangle_I$.

Figure 8(a) shows the conditional mean vorticity magnitude $\langle\omega\rangle_I$ at $Re_\theta = 2000$ in the FG. $\langle\omega\rangle_I$ is compared among irrotational boundaries detected with different threshold values in the range of $0.65\omega_{th0}$ to $1.5\omega_{th0}$, where these values correspond to the vertical broken lines in Fig. 6. $\langle\omega\rangle_I$ sharply decreases from the turbulent region to the irrotational boundary. This is hardly affected by the choice of ω_{th} for $0.65\omega_{th0} \le \omega_{th} \le 1.5\omega_{th0}$. The following analysis is based on the irrotational boundary detected with $\omega_{th} = \omega_{th0}$. Figure 8(b) compares $\langle\omega\rangle_I$ computed with different values of Δ_ζ (see Fig. 7). Since $\langle\omega\rangle_I$ does not change with Δ_ζ, $\Delta_\zeta = 15\eta_r$ is used hereafter.

D. Different detector functions for turbulent fluids

Experimental measurements of the vorticity magnitude, i.e., three components of the vorticity vector, are difficult. Therefore, the detection of turbulent fluids from intermittent flows often relies on other quantities that characterize turbulent fluids. Recent studies[36,45,69] have used spanwise vorticity magnitude $|\omega_z|$, local (turbulent) kinetic energy $k = (u^2 + v^2 + w^2)/2$, or passive scalar ϕ as a detection function of turbulent fluids d, where turbulent fluids are detected as $d \ge d_{th}$.

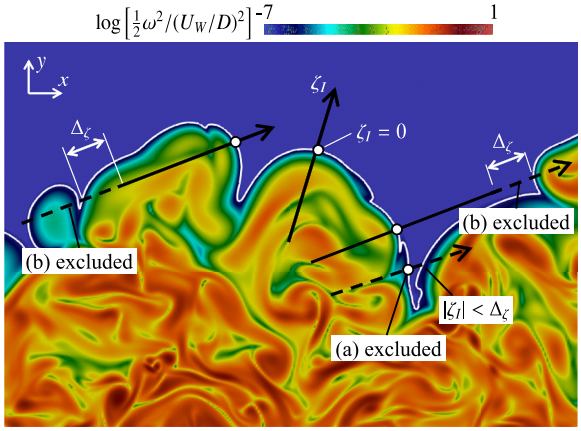

FIG. 7. Computation of statistics conditioned on distance from the irrotational boundary (shown with a white line). Local interface coordinate ζ_I can be defined for each location of the irrotational boundary with its origin (shown as circles) at the irrotational boundary. Locations on ζ_I shown with broken lines are excluded from conditional statistics.

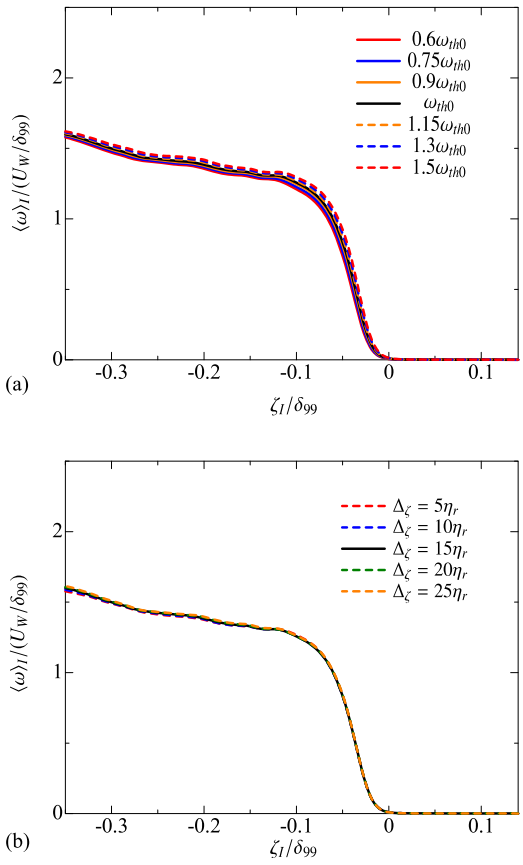

FIG. 8. Conditional mean vorticity magnitude $\langle\omega\rangle_I$: influence of (a) threshold for detecting irrotational boundary and (b) length of a region excluded from conditional statistics, Δ_ζ. Results are taken from the FG at $Re_\theta = 2000$.

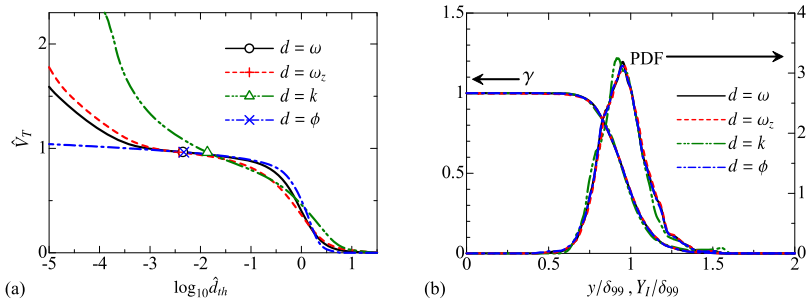

FIG. 9. (a) Turbulent volume detected by different detector functions d as a function of threshold d_{th}, where $\hat{d}_{th}$ denotes d_{th} normalized by mean value of d at $y/\delta_{99} = 0.5$. d is vorticity magnitude ω, spanwise vorticity magnitude $|\omega_z|$, kinetic energy k, or passive scalar ϕ. Thresholds used for detecting the irrotational boundary are marked with symbols. (b) Intermittency factor γ and the PDF of irrotational boundary height Y_I for different detector functions d. Results are taken from the FG at $Re_\theta = 2000$.

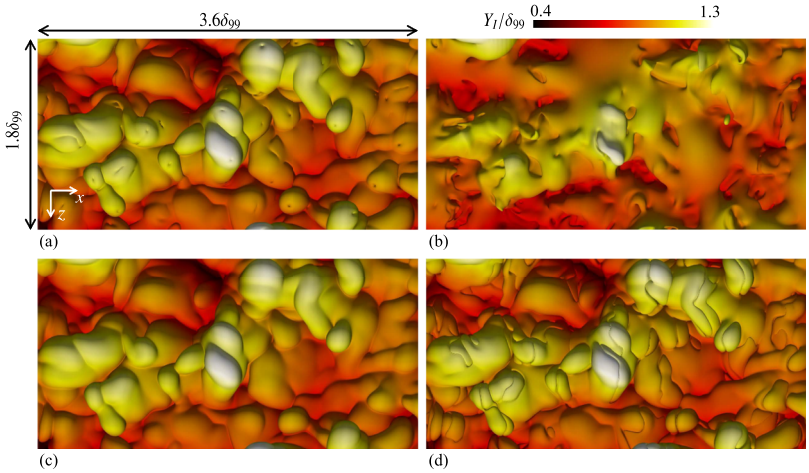

FIG. 10. Top view of the isosurface detected for investigating the TNTI by (a) vorticity magnitude ω, (b) kinetic energy k, (c) passive scalar ϕ, and (d) spanwise vorticity magnitude $|\omega_z|$. The isosurface is colored by vertical height Y_I divided by boundary layer thickness δ_{99}. Results are taken from the FG at $Re_\theta = 2000$.

Figure 9(a) compares the normalized turbulent volume $\hat{V}_T$ as a function of d_{th} for $d = \omega$, $|\omega_z|$, k, and ϕ, where d_{th} is normalized by the mean value of d at $y/\delta_{99} = 0.5$, i.e., $\hat{d}_{th} = d_{th}/\langle d \rangle_r$. The dependence of $\hat{V}_T$ on the threshold is similar for ω, $|\omega_z|$, and ϕ, where there is a range of threshold for which $\hat{V}_T$ exhibits a weak dependence on the threshold. However, $\hat{V}_T$ computed with k keeps increasing as the threshold is decreased. d_{th} for $|\omega_z|$, k, and ϕ is determined so that the turbulent volume is equal to $\hat{V}_T$ detected by the vorticity magnitude with ω_{th0}. These threshold values are marked with symbols in Fig. 9(a). They are used for computing the intermittency factor γ, a probability that a turbulent fluid is found at y, and the PDF of the wall normal position of the isosurface $d = d_{th}$ denoted by Y_I, as depicted in Fig. 9(b). Both the intermittency factor and PDF of Y_I are insensitive to the choice of d considered here. A small deviation from the results with $d = \omega$ can be found for the interface detected with the kinetic energy.

Figure 10 shows the top view of isosurface $d = d_{th}$ ($Re_\theta = 2000$), while the isosurface on an x-y plane is compared with enstrophy in Fig. 11. The isosurface is similar except for $d = k$. The shape of the isosurface is different between $d = \omega$ and k even though the isosurface of k and ω appears at a similar height. It is also found that passive scalar and spanwise vorticity are good markers of turbulent fluids detected

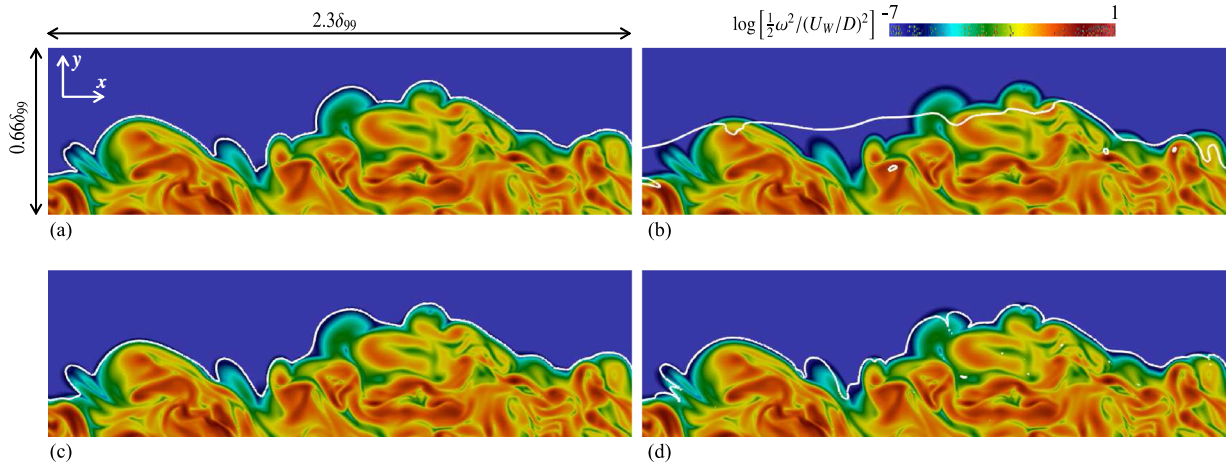

FIG. 11. Enstrophy field (color contour) and isosurface (white line) detected for investigating the TNTI by (a) vorticity magnitude ω, (b) kinetic energy k, (c) passive scalar ϕ, and (d) spanwise vorticity magnitude $|\omega_z|$. Results are taken from the FG at $Re_\theta = 2000$.

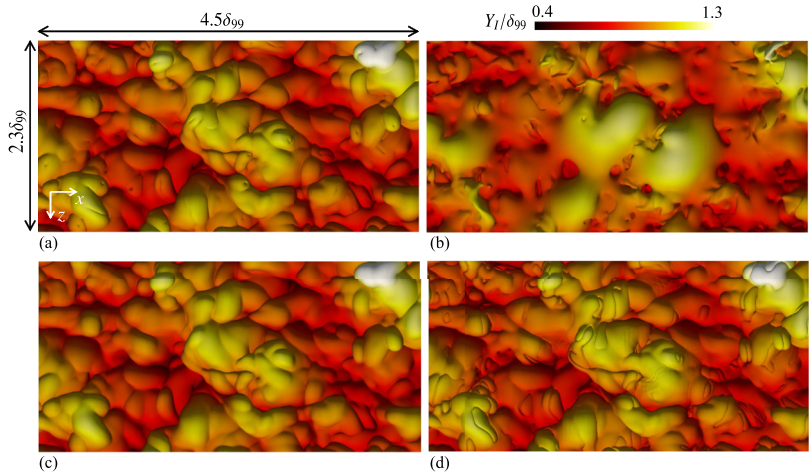

FIG. 12. The same as in Fig. 10 but obtained at $Re_\theta = 1700$.

with the vorticity magnitude. A similar difference between $d = k$ and others can be found at $Re_\theta = 1700$ as visualized in Fig. 12. The significant difference in the isosurface between $d = \omega$ and k is explained by different mechanisms that contribute to the spatial transport of vorticity and kinetic energy. Non-turbulent fluids gain vorticity by viscous diffusion, which acts locally in the vicinity of the TNTI layer.[22] However, the kinetic energy transfer from turbulent to non-turbulent fluids is caused by both viscous diffusion and pressure diffusion, where the pressure diffusion can affect the kinetic energy of non-turbulent fluids even far away from the TNTI layer.[70–72] This pressure effect, which is absent in the enstrophy transport equation, causes the different distribution between the kinetic energy and enstrophy.

Figure 13 shows the conditional average of the vorticity magnitude, second invariant of the velocity gradient tensor, $Q = (\omega_i\omega_i - 2S_{ij}S_{ij})/4$, and streamwise velocity u computed with the distance from the isosurface $d = d_{th}$, where S_{ij} is the rate of strain tensor. The isosurface of the passive scalar or spanwise vorticity magnitude yields the conditional statistics consistent with the results for the isosurface of the vorticity magnitude. Since the distribution of vorticity is not well captured by the kinetic energy, the conditional vorticity magnitude computed with $d = k$ does not exhibit a sharp jump across the TNTI layer. $\langle Q\rangle_I$ in Fig. 13 is also different for $d = k$: $\langle Q\rangle_I$ with $d = k$ is close to 0 even within the TNTI layer while $\langle Q\rangle_I$ exhibits negative and positive peaks for $d = \omega$, $|\omega_z|$, and ϕ. These negative and positive peaks are found near the TNTI in free shear flows[39,56] and are related to the vortical structures near the TNTI,[73] where the core of the vortex has $Q > 0$ while $Q < 0$ can be found in the region surrounding the core.[74] The difference in $\langle u\rangle_I$ among different detector functions of turbulent fluids is smaller than that in $\langle\omega\rangle_I$ and $\langle Q\rangle_I$. However, $\langle u\rangle_I$, except for $d = k$, increases from $\zeta_I \approx -0.05\delta_{99}$ toward the turbulent core region while $\langle u\rangle_I$ detected with $d = k$ start to deviate from the non-turbulent value at $\zeta_I = 0$.

These results confirm that the characteristics of the TNTI layer studied with the isosurface of the vorticity magnitude are well captured with the isosurface of the spanwise vorticity magnitude or passive scalar, which are often available in experiments of turbulent boundary layers.

E. Turbulent statistics characterizing TNTI

Turbulent statistics that characterize the TNTI are explored here. It is important to consider the statistical properties of turbulent fluids in the intermittent region because the non-turbulent fluids have a different nature from turbulence. The average of turbulent fluids $\langle f\rangle_T$ can be defined with an intermittency function I,[75]

$$\langle f\rangle_T(y;t) = \frac{\langle I(x,y,z;t)f(x,y,z;t)\rangle}{\langle I(x,y,z;t)\rangle}, \tag{9}$$

$$I(x,y,z;t) = \begin{cases} 1 & \text{for } \omega \geq \omega_{th0} \text{ (turbulent fluid)} \\ 0 & \text{for } \omega < \omega_{th0} \text{ (non-turbulent fluid)} \end{cases}. \tag{10}$$

As can be seen in Fig. 5(b), the length scale of turbulent structures varies depending on the distance from the wall. The Kolmogorov length scale of turbulent fluids, η_T, can be

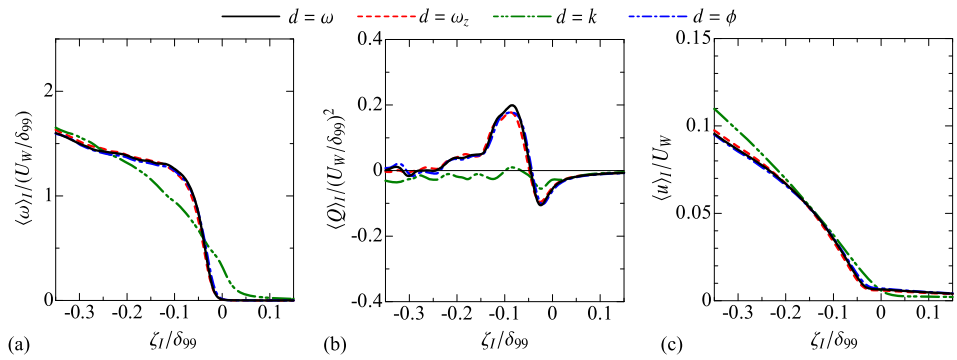

FIG. 13. Conditional averages of (a) vorticity magnitude ω, (b) second invariant of velocity gradient tensor Q, and (c) streamwise velocity u. Conditional statistics are compared with the isosurface of vorticity magnitude ω, spanwise vorticity magnitude $|\omega_z|$, kinetic energy k, and passive scalar ϕ. Results are taken from the FG at $Re_\theta = 2000$.

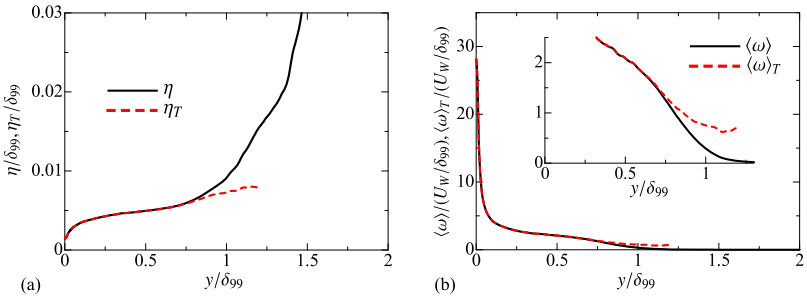

FIG. 14. Vertical profiles of the (a) Kolmogorov scale and (b) vorticity magnitude in the FG at $Re_\theta = 2000$. Statistics computed only from turbulent fluids are compared with conventional statistics based on the spatial average on x-z planes.

defined with the averaged kinetic energy dissipation rate of turbulent fluids $\langle\varepsilon\rangle_T$ as $\eta_T = (\nu^3/\langle\varepsilon\rangle_T)^{1/4}$, which is compared in Fig. 14(a) with Kolmogorov length scale $\eta = (\nu^3/\langle\varepsilon\rangle)^{1/4}$ including the contributions from turbulent and non-turbulent fluids ($\varepsilon = 2\nu S_{ij}S_{ij}$). In the intermittent region with $0 < \gamma < 1$, η_T is smaller than η because of the low kinetic energy dissipation rate of non-turbulent fluids.[39] Similarly, a vertical profile of $\langle\omega\rangle_T$ is plotted in comparison with $\langle\omega\rangle$ in Fig. 14(b). $\langle\omega\rangle_T$ does not approach 0 even for large y. Even though the non-turbulent fluids are excluded from the average, $\langle\omega\rangle_T$ strongly depends on y, confirming that the characteristics of turbulence depend on the wall normal direction.

The conditional statistics of the TNTI need to be normalized by appropriate quantities for comparing the TNTI in different flows. Since the TNTI appears in the outermost region of turbulent boundary layers, the normalization should be based on the characteristics of turbulence in the vicinity of the TNTI rather than the near wall region. Here, the statistics computed with an average of turbulent fluids in the intermittent region are defined as

$$\langle f\rangle_{TI}(t) = \frac{\iiint I_{TI}(x,y,z;t) f(x,y,z;t)\mathrm{d}x\mathrm{d}y\mathrm{d}z}{\iiint I_{TI}(x,y,z;t)\mathrm{d}x\mathrm{d}y\mathrm{d}z}, \tag{11}$$

$$I_{TI}(x,y,z;t) = \begin{cases} 1 & \text{for } \omega \geq \omega_{th0} \text{ and } 0 < \gamma < 1 \\ 0, & \text{otherwise} \end{cases}, \tag{12}$$

where I_{TI} is equal to 1 for turbulent fluids that appear in the intermittent region. The Kolmogorov scale can also be defined with $\langle\varepsilon\rangle_{TI}$ as $\eta_{TI} = (\nu^3/\langle\varepsilon\rangle_{TI})^{1/4}$. Similarly, the Taylor microscale can be defined with turbulent kinetic energy $k_{TI} = (\langle u_i u_i\rangle_{TI} - \langle u_i\rangle_{TI}\langle u_i\rangle_{TI})/2$ as $\lambda_T = (10\nu k_{TI}/\langle\varepsilon\rangle_{TI})^{1/2}$. The mean vorticity magnitude in the intermittent region can also be obtained as $\langle\omega\rangle_{TI}$.

The conditional statistics are compared between the turbulent boundary layer and planar jet. The DNS database of the temporally developing planar jet is taken from our previous paper.[58] The DNS of the planar jet is briefly described here. The mean flow direction is represented by x, while the direction in which the planar jet spreads is referred to as the y direction. The spanwise direction, which is orthogonal to both x and y coordinates, is represented by z. The DNS of the temporally developing planar jet is initialized with a mean velocity profile given by

$$\langle u\rangle(y, t=0) = \frac{1}{2}U_J + \frac{1}{2}U_J \tanh\left(\frac{H - 2|y|}{4\theta_J}\right), \tag{13}$$

$$\langle v\rangle(y, t=0) = \langle w\rangle(y, t=0) = 0, \tag{14}$$

where u, v, and w are streamwise (x), cross-streamwise (y), and spanwise (z) components of the velocity vector, respectively, and U_J is the jet velocity, H is the slit width, and $\theta_J = 0.015H$ is the initial shear layer thickness. Fluctuating components with rms values of $0.02U_J$ and a characteristic length scale of $0.2H$ generated by a diffusive process[51] are superimposed on the mean velocity. The jet Reynolds number is $Re_J = U_J H/\nu = 10\,000$, for which turbulent Reynolds number Re_λ defined with streamwise velocity is about 120 in a self-similar regime on the jet centerline. The jet develops in the computational domain with the size of $(L_x \times L_y \times L_z) = (6H \times 10H \times 4H)$, which is represented by $(N_x \times N_y \times N_z) = (1200 \times 1600 \times 800)$ grid points. The DNS code is the same as the one used for the turbulent boundary layer in the present study except for the boundary/initial conditions. Figure 15 visualizes enstrophy in the planar jet in a self-similar regime at $t = 16(H/U_J)$. Comparison with Fig. 5(b) shows that the structures of the strong vorticity region are less sensitive to the cross-streamwise location in the planar jets than in the turbulent boundary layer, where these structures are influenced by the wall. Figure 15(b) shows the cross-streamwise profiles of the intermittency factor γ and Kolmogorov length scale (η and η_T). Here, the irrotational

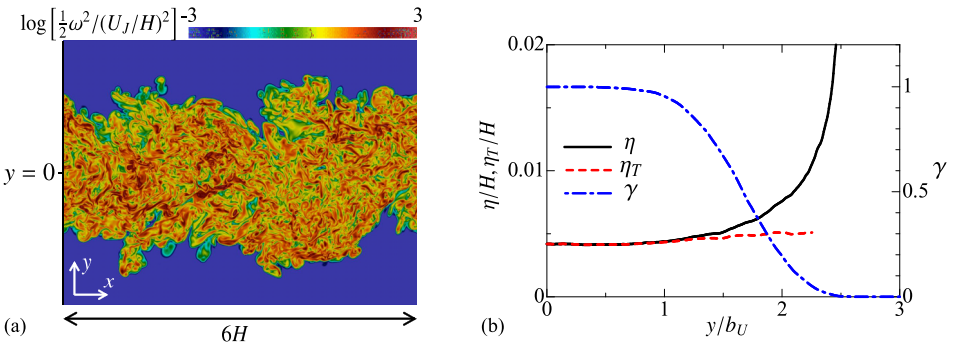

FIG. 15. (a) Enstrophy profile on an x-y plane in the planar jet. (b) Intermittency factor γ and Kolmogorov length scales (η and η_T) in the planar jet, where y is normalized by a jet half-width of mean streamwise velocity.

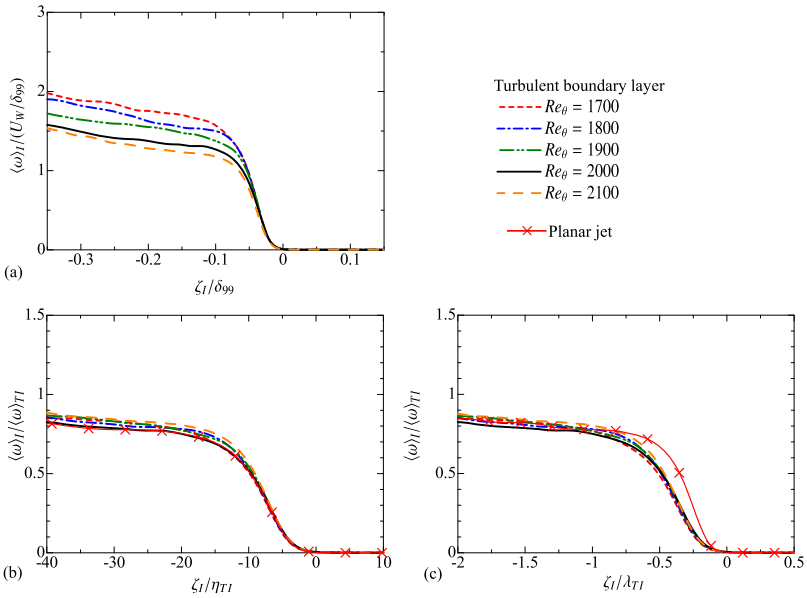

FIG. 16. (a) Conditional mean vorticity magnitude at different Re_θ. The normalized profile of the conditional mean vorticity magnitude in the turbulent boundary layer at different Re_θ and planar jet plotted with the interface coordinate normalized by (b) Kolmogorov length scale η_{TI} and (c) Taylor microscale λ_{TI} of turbulent fluids in an intermittent region.

boundary is detected as $\omega = \omega_{th0}$. In the intermittent region with $0 < \gamma < 1$, the Kolmogorov scale of turbulent fluids η_T is smaller than η computed from both turbulent and non-turbulent fluids. However, unlike the turbulent boundary layer, η_T exhibits only a small variation in the y direction.

Conditional mean vorticity magnitude $\langle\omega\rangle_I$ is compared at different Re_θ (time) in the turbulent boundary layer and in the planar jet. Figure 16(a) shows $\langle\omega\rangle_I$ in the turbulent boundary layer in the range of $1700 \le Re_\theta \le 2100$, where $\langle\omega\rangle_I$ and ζ_I are normalized by U_W/δ_{99} and δ_{99}, respectively. $\langle\omega\rangle_I$ plotted in this way depends on Re_θ: $\langle\omega\rangle_I$ decreases with Re_θ, which increases with time. Figures 16(b) and 16(c) show the results normalized by the statistics of the turbulent fluids in the intermittent region of the turbulent boundary layer and planar jet, where $\langle\omega\rangle_I/\langle\omega\rangle_{TI}$ is plotted against ζ_I/η_{TI} or ζ_I/λ_{TI}. $\langle\omega\rangle_I/\langle\omega\rangle_{TI}$ collapses onto a single curve when ζ_I is normalized by η_{TI}, indicating that the thickness of the TNTI layer scales with the Kolmogorov length scale. The thickness of the TNTI layer normalized by the Taylor microscale is smaller for the planar jet than for the turbulent boundary layer.

The inner structure of the TNTI layer is often examined with the enstrophy transport equation,

$$\frac{D\omega^2/2}{Dt} = \omega_i S_{ij}\omega_j - \nu\frac{\partial\omega_i}{\partial x_j}\frac{\partial\omega_i}{\partial x_j} + \nu\frac{\partial^2\omega^2/2}{\partial x_j\partial x_j}, \qquad (15)$$

where the first, second, and third terms represent enstrophy production P_ω, viscous dissipation ε_ω, and viscous diffusion D_ω. The conditional average of these terms is compared between the turbulent boundary layer and planer jet in Fig. 17, where the enstrophy budget is normalized with a mean strain product of turbulent fluids in the intermittent region $\langle S_{ij}S_{ij}\rangle_{TI}$ while ζ_I is normalized by η_{TI}. The enstrophy budget normalized in this way shows good agreement between the turbulent boundary layer and planar jet. These results confirm that the turbulence characteristics of the intermittent region well characterize the small-scale statistics, such as vorticity, near the TNTI in different flows.

Figure 18(a) shows conditional mean velocity magnitude $\langle|\boldsymbol{u}|\rangle_I$ normalized by U_W. $\langle|\boldsymbol{u}|\rangle_I$ rapidly changes for $-20 \le \zeta_I/\eta_{TI} \le -10$ while the slope of $\langle|\boldsymbol{u}|\rangle_I$ is less steep for $\zeta_I/\eta_{TI} \le -20$. In Fig. 18(b), $\langle|\boldsymbol{u}|\rangle_I$ is normalized by $(2k_{TI}/3)^{1/2}$, which is related to rms velocity fluctuations of turbulent fluids in the intermittent region. It is found that $\langle|\boldsymbol{u}|\rangle_I$ reaches $\langle|\boldsymbol{u}|\rangle_I/(2k_{TI}/3)^{1/2} \approx 1$ at $\zeta_I/\eta_{TI} = -20$. Conditional mean streamwise velocity in the DNS of the turbulent boundary layer also exhibits a velocity jump near the TNTI layer, whose magnitude is similar to rms velocity fluctuation in the turbulent boundary layer.[31]

F. Spatial resolution effects on the TNTI layer

Figure 19 shows the grid spacing Δ_i ($i = x, y$, and z) divided by the Kolmogorov scale of turbulent fluids $\eta_T(y)$ in the present DNS. The DNS with the CG in Fig. 19(a) has a grid spacing of $\Delta_x \approx 2\text{-}3\eta_T$ in the outer region, which is larger than recent DNS studies of the TNTI in free shear flows.[22,23] In contrast, the FG and VFG yield $\Delta_x = \Delta_z \approx 1.0\text{-}1.5\eta_T$ and $\Delta_x = \Delta_z \approx 0.6\text{-}1.0\eta_T$ in the outer region, respectively. It should be noted that the CG

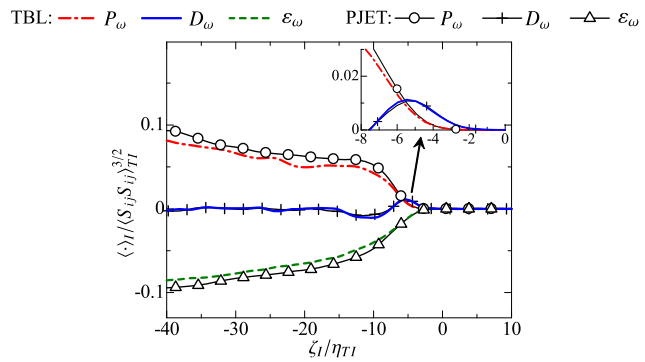

FIG. 17. Conditional budget of enstrophy near the TNTI in the turbulent boundary layer (TBL) and planar jet (PJET). Each term is normalized with a mean strain product of turbulent fluids in an intermittent region while ζ_I is normalized by Kolmogorov length scale η_{TI}.

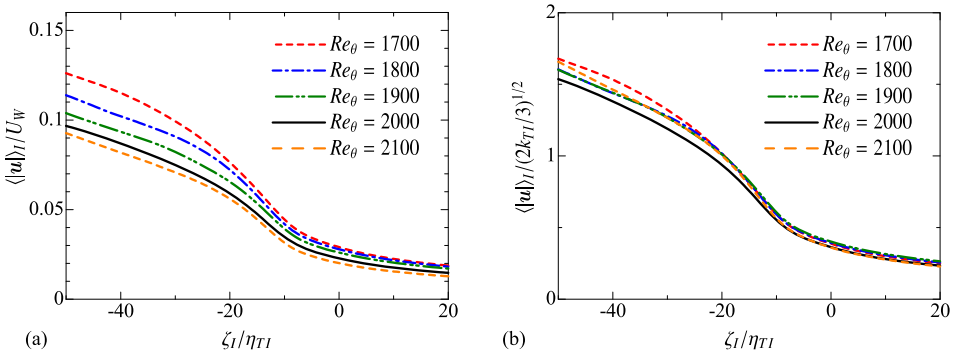

FIG. 18. Conditional mean velocity magnitude $\langle|\boldsymbol{u}|\rangle_I$ at different Re_θ plotted against the interface coordinate normalized by Kolmogorov length scale η_{TI}. $\langle|\boldsymbol{u}|\rangle_I$ is normalized by (a) U_W and (b) $(2k_{TI}/3)^{1/2}$.

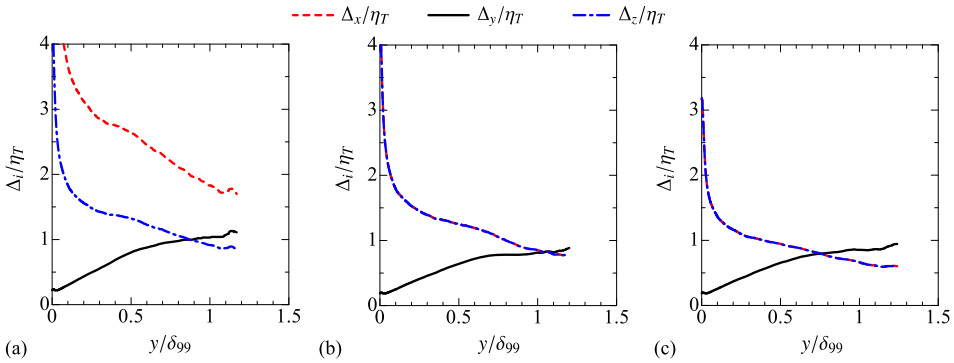

FIG. 19. Size of the computational grid in relation to Kolmogorov length scale η_T of turbulent fluids in the (a) CG, (b) FG, and (c) VFG at $Re_\theta = 2000$.

has Δ_x small enough to satisfy the criteria that is widely used in the DNS of wall turbulence as summarized in Table I. These results clearly confirm that the grid spacing determined solely by the wall unit is too coarse to resolve the smallest scales of turbulence in the outer region. The grid in the outer region in the FG yields the spatial resolution close to the previous DNS of free shear flows.[70] The region very close to the wall has large values of Δ_x/η_T and Δ_z/η_T. However, the near-wall region is governed by anisotropic structures elongated in the streamwise direction, and the grid spacing near the wall should be compared in terms of the wall unit as in previous DNS studies of wall turbulence.

Figure 20(a) compares the conditional average of vorticity magnitude $\langle\omega\rangle_I$ among the DNS with different spatial resolutions. Since the TNTI layer is characterized by a large gradient of $\langle\omega\rangle_I$, $\omega_I' = \mathrm{d}\langle\omega\rangle_I/\mathrm{d}\zeta_I$ is also shown in the figure. The influence of the resolution is not significant in the profile of $\langle\omega\rangle_I$. However, the DNS with the CG slightly underestimates a peak in $-\omega_I'$, indicating that the vorticity profile across the TNTI layer is smoothed.

One of the important quantities that characterize the geometry of the TNTI is the mean curvature defined as $H_C = \nabla \cdot \mathbf{n}/2$. Local entrainment velocity defined as a propagation velocity of the enstrophy isosurface strongly depends on H_C.[27] In the present definition of H_C, $H_C > 0$ represents a convex shape in a top view of the irrotational boundary. Figure 20(b) compares the PDF of H_C among the CG, FG, and VFG. A peak of the PDF appears for $H_C > 0$ while a long tail can be seen for negative H_C. The influence of spatial resolution is clear for the PDF of H_C: a probability for large negative H_C is larger for the CG. Figure 21 compares a top view of the irrotational boundary colored by H_C between the CG and FG. A large part of the irrotational boundary is characterized by a convex shape with small and positive H_C. Convex regions with $H_C > 0$ are separated by thin and long concave regions with large and negative H_C. The influence of the spatial resolution is clearly seen around the concave regions with $H_C < 0$: unnatural spiky patterns with large positive and negative H_C are visible for the CG in Fig. 21(a). These patterns are mostly orthogonal to the streamwise direction, for which the spatial resolution is insufficient in the CG. The grid spacing with $\Delta_x \approx 2\Delta_z \approx 8(\nu/u_\tau)$ widely used in the simulations of wall turbulence results in an insufficient resolution in the outer region of the turbulent boundary layer. Even though the

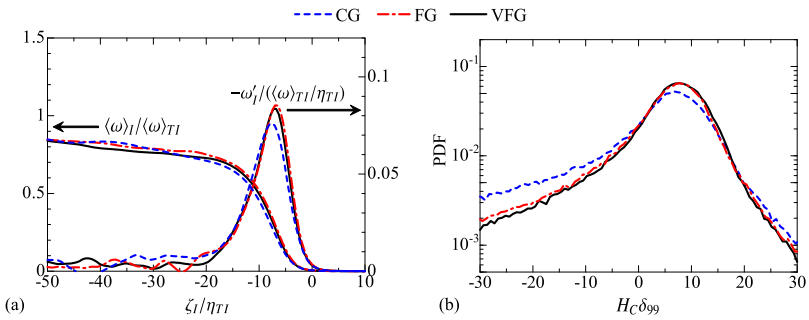

FIG. 20. Influence of spatial resolution on the TNTI at $Re_\theta = 2000$: (a) conditional mean vorticity magnitude and its derivative with respective to ζ_I and (b) PDF of the mean curvature of the irrotational boundary.

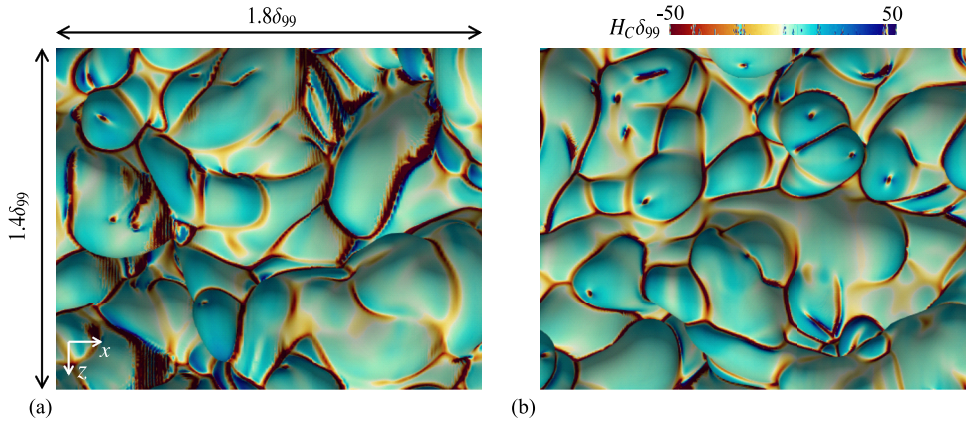

FIG. 21. Top view of the irrotational boundary colored by mean curvature H_C in (a) the CG and (b) FG.

DNS with $\Delta_x \approx 2\Delta_z$ in the CG provides the vertical profiles of mean velocity and rms velocity fluctuations consistent with the DNS with better spatial resolutions, the influence of insufficient spatial resolution in the outer region cannot be neglected in the geometry of the TNTI.

IV. CONCLUSION

The DNS of temporally developing turbulent boundary layers is performed for $Re_\theta \approx 2000$ for studying the TNTI that appears in the intermittent region of the boundary layers. It is shown that the outer edge of the TNTI layer is well detected as the isosurface of vorticity magnitude with the threshold determined with the dependence of the turbulent volume on a threshold level.

Various quantities have been used as a detector function of turbulent fluids in previous studies although the influence of the detector function is not well known for the conditional statistics for the TNTI. We test the vorticity magnitude, spanwise vorticity magnitude, passive scalar, and local kinetic energy as a detector function of turbulent fluids in the turbulent boundary layer. The spanwise vorticity magnitude and passive scalar are good markers of turbulent fluids. The usage of spanwise vorticity or passive scalar hardly affects the conditional statistics. However, the TNTI cannot be detected by thresholding kinetic energy even though the intermittency factor exhibits good agreement between turbulent fluids detected with the kinetic energy and vorticity magnitude. The conditional statistics also significantly differ between the TNTI detected by the kinetic energy and vorticity magnitude when the quantities related to small-scales are of interest.

Most previous DNSs of turbulent boundary layers have determined the spatial resolution in comparison with the length scale of the near-wall region although the structure of turbulence varies depending on the wall-normal direction. The influence of the spatial resolution on the TNTI is studied by comparing the DNS with three different grid settings, all of which satisfy the criteria widely used in the DNS of wall turbulence. The spatial resolutions are compared with the Kolmogorov length scale computed for turbulent fluids. The grid setting determined solely from the wall unit ($\Delta_x^+ \approx 9$) results in an insufficient resolution in a streamwise direction in the outer region, which causes spiky patterns of the irrotational boundary with unnaturally large positive and negative values of mean curvature. A smooth irrotational boundary can be obtained in the DNS when the number of the grid points in the streamwise direction is increased by a factor of two, which yields $\Delta_x^+ \approx \Delta_z^+ \approx 5$.

The TNTI characteristics are compared between the turbulent boundary layer and planar jet. The dependence of turbulence characteristics on the cross-streamwise location is stronger in the turbulent boundary layer than in the planar jet. The characteristics of turbulence in the vicinity of the TNTI layer are computed with the statistics of turbulent fluids in the intermittent region, which are used in normalization of the conditional statistics for comparing the two flows. The normalized statistics plotted against the distance from the irrotational boundary divided by the Kolmogorov length scale show good quantitative agreement between the turbulent boundary layer and planar jet. These normalizations enable us to investigate universality of the TNTI layer characteristics in different flows.

ACKNOWLEDGMENTS

The authors would like to acknowledge Professor C. B. da Silva for stimulating discussions. The numerical simulations presented in this manuscript were carried out on the high-performance computing system (NEC SX-ACE) in the Japan Agency for Marine-Earth Science and Technology. This work was partially supported by "Collaborative Research Project on Computer Science with High-Performance Computing in Nagoya University" and by MEXT KAKENHI Grant No. 16K18013.

[1]D. Coles, "The law of the wake in the turbulent boundary layer," J. Fluid Mech. **1**, 191 (1956).
[2]P. Bradshaw and G. P. Huang, "The law of the wall in turbulent flow," Proc. R. Soc. A **451**, 165 (1995).
[3]H. H. Fernholz and P. J. Finleyt, "The incompressible zero-pressure-gradient turbulent boundary layer: An assessment of the data," Prog. Aeronaut. Sci. **32**, 245 (1996).
[4]A. A. Townsend, "The structure of the turbulent boundary layer," Math. Proc. Cambridge Philos. Soc. **47**, 375 (1951).
[5]S. K. Robinson, "Coherent motions in the turbulent boundary layer," Annu. Rev. Fluid Mech. **23**, 601 (1991).
[6]R. J. Adrian, "Hairpin vortex organization in wall turbulence," Phys. Fluids **19**, 041301 (2007).
[7]M. Gad-el Hak and P. R. Bandyopadhyay, "Reynolds number effects in wall-bounded turbulent flows," Appl. Mech. Rev. **47**, 307 (1994).

[8]I. Marusic, B. J. McKeon, P. A. Monkewitz, H. M. Nagib, A. J. Smits, and K. R. Sreenivasan, "Wall-bounded turbulent flows at high Reynolds numbers: Recent advances and key issues," Phys. Fluids **22**, 065103 (2010).
[9]A. J. Smits, B. J. McKeon, and I. Marusic, "High–Reynolds number wall turbulence," Annu. Rev. Fluid Mech. **43**, 353 (2011).
[10]J. Jiménez, "Cascades in wall-bounded turbulence," Annu. Rev. Fluid Mech. **44**, 27 (2012).
[11]J. Jiménez, "Turbulent flows over rough walls," Annu. Rev. Fluid Mech. **36**, 173 (2004).
[12]R. E. Falco, "Coherent motions in the outer region of turbulent boundary layers," Phys. Fluids **20**, S124 (1977).
[13]R. A. Antonia, "Conditional sampling in turbulence measurement," Annu. Rev. Fluid Mech. **13**, 131 (1981).
[14]S. Corrsin and A. L. Kistler, "Free-stream boundaries of turbulent flows," NACA Technical Report No. TN-1244, 1955.
[15]L. S. G. Kovasznay, V. Kibens, and R. F. Blackwelder, "Large-scale motion in the intermittent region of a turbulent boundary layer," J. Fluid Mech. **41**, 283 (1970).
[16]T. B. Hedleyt and J. F. Keffer, "Some turbulent/non-turbulent properties of the outer intermittent region of a boundary layer," J. Fluid Mech. **64**, 645 (1974).
[17]J. C. LaRue and P. A. Libby, "Temperature fluctuations in the plane turbulent wake," Phys. Fluids **17**, 1956 (1974).
[18]R. A. Antonia, A. Prabhu, and S. E. Stephenson, "Conditionally sampled measurements in a heated turbulent jet," J. Fluid Mech. **72**, 455 (1975).
[19]E. Gutmark and I. Wygnanski, "The planar turbulent jet," J. Fluid Mech. **73**, 465 (1976).
[20]C. B. da Silva, J. C. R. Hunt, I. Eames, and J. Westerweel, "Interfacial layers between regions of different turbulence intensity," Annu. Rev. Fluid Mech. **46**, 567 (2014).
[21]D. K. Bisset, J. C. R. Hunt, and M. M. Rogers, "The turbulent/non-turbulent interface bounding a far wake," J. Fluid Mech. **451**, 383 (2002).
[22]R. R. Taveira and C. B. da Silva, "Characteristics of the viscous superlayer in shear free turbulence and in planar turbulent jets," Phys. Fluids **26**, 021702 (2014).
[23]M. van Reeuwijk and M. Holzner, "The turbulence boundary of a temporal jet," J. Fluid Mech. **739**, 254 (2014).
[24]J. Westerweel, C. Fukushima, J. M. Pedersen, and J. C. R. Hunt, "Mechanics of the turbulent-nonturbulent interface of a jet," Phys. Rev. Lett. **95**, 174501 (2005).
[25]M. Holzner, A. Liberzon, N. Nikitin, B. Lüthi, W. Kinzelbach, and A. Tsinober, "A Lagrangian investigation of the small-scale features of turbulent entrainment through particle tracking and direct numerical simulation,"J. Fluid Mech. **598**, 465 (2008).
[26]M. Holzner and B. Lüthi, "Laminar superlayer at the turbulence boundary," Phys. Rev. Lett. **106**, 134503 (2011).
[27]M. Wolf, M. Holzner, B. Lüthi, D. Krug, W. Kinzelbach, and A. Tsinober, "Effects of mean shear on the local turbulent entrainment process," J. Fluid Mech. **731**, 95 (2013).
[28]R. R. Taveira, J. S. Diogo, D. C. Lopes, and C. B. da Silva, "Lagrangian statistics across the turbulent-nonturbulent interface in a turbulent plane jet," Phys. Rev. E **88**, 043001 (2013).
[29]T. Watanabe, C. B. da Silva, Y. Sakai, K. Nagata, and T. Hayase, "Lagrangian properties of the entrainment across turbulent/non-turbulent interface layers," Phys. Fluids **28**, 031701 (2016).
[30]R. Jahanbakhshi and C. K. Madnia, "Entrainment in a compressible turbulent shear layer," J. Fluid Mech. **797**, 564 (2016).
[31]T. Ishihara, H. Ogasawara, and J. C. R. Hunt, "Analysis of conditional statistics obtained near the turbulent/non-turbulent interface of turbulent boundary layers," J. Fluids Struct. **53**, 50 (2015).
[32]J. C. R. Hunt and P. A. Durbin, "Perturbed vortical layers and shear sheltering," Fluid Dyn. Res. **24**, 375 (1999).
[33]G. Borrell and J. Jiménez, "Properties of the turbulent/non-turbulent interface in boundary layers," J. Fluid Mech. **801**, 554 (2016).
[34]J. Lee, H. J. Sung, and T. A. Zaki, "Signature of large-scale motions on turbulent/non-turbulent interface in boundary layers," J. Fluid Mech. **819**, 165 (2017).
[35]C. M. de Silva, J. Philip, K. Chauhan, C. Meneveau, and I. Marusic, "Multiscale geometry and scaling of the turbulent-nonturbulent interface in high Reynolds number boundary layers," Phys. Rev. Lett. **111**, 044501 (2013).
[36]K. Chauhan, J. Philip, C. M. de Silva, N. Hutchins, and I. Marusic, "The turbulent/non-turbulent interface and entrainment in a boundary layer," J. Fluid Mech. **742**, 119 (2014).
[37]J. Philip, C. Meneveau, C. M. de Silva, and I. Marusic, "Multiscale analysis of fluxes at the turbulent/non-turbulent interface in high Reynolds number boundary layers," Phys. Fluids **26**, 015105 (2014).
[38]M. Kozul, D. Chung, and J. P. Monty, "Direct numerical simulation of the incompressible temporally developing turbulent boundary layer," J. Fluid Mech. **796**, 437 (2016).
[39]C. B. da Silva and J. C. F. Pereira, "Invariants of the velocity-gradient, rate-of-strain, and rate-of-rotation tensors across the turbulent/nonturbulent interface in jets," Phys. Fluids **20**, 055101 (2008).
[40]M. M. Rogers and R. D. Moser, "Direct simulation of a self-similar turbulent mixing layer," Phys. Fluids **6**, 903 (1994).
[41]M. Gampert, J. Boschung, F. Hennig, M. Gauding, and N. Peters, "The vorticity versus the scalar criterion for the detection of the turbulent/non-turbulent interface," J. Fluid Mech. **750**, 578 (2014).
[42]R. Jahanbakhshi, N. S. Vaghefi, and C. K. Madnia, "Baroclinic vorticity generation near the turbulent/non-turbulent interface in a compressible shear layer," Phys. Fluids **27**, 105105 (2015).
[43]T. Watanabe, Y. Sakai, K. Nagata, Y. Ito, and T. Hayase, "Turbulent mixing of passive scalar near turbulent and non-turbulent interface in mixing layers," Phys. Fluids **27**, 085109 (2015).
[44]C. S. Subramanian and R. A. Antonia, "Effect of Reynolds number on a slightly heated turbulent boundary layer," Int. J. Heat Mass Transfer **24**, 1833 (1981).
[45]J. Eisma, J. Westerweel, G. Ooms, and G. E. Elsinga, "Interfaces and internal layers in a turbulent boundary layer," Phys. Fluids **27**, 055103 (2015).
[46]C.-H. P. Chen and R. F. Blackwelder, "Large-scale motion in a turbulent boundary layer: A study using temperature contamination," J. Fluid Mech. **89**, 1 (1978).
[47]R. D. Moser, J. Kim, and N. N. Mansour, "Direct numerical simulation of turbulent channel flow up to $Re_\tau = 590$," Phys. Fluids **11**, 943 (1999).
[48]N. Rostamy, D. J. Bergstrom, D. Sumner, and J. D. Bugg, "The effect of surface roughness on the turbulence structure of a plane wall jet," Phys. Fluids **23**, 085103 (2011).
[49]M. Aamir and Z. Ahmad, "Review of literature on local scour under plane turbulent wall jets," Phys. Fluids **28**, 105102 (2016).
[50]M. Aamir and Z. Ahmad, *Development of Water Resources in India* (Springer, 2017), pp. 375–385.
[51]A. Kempf, M. Klein, and J. Janicka, "Efficient generation of initial-and inflow-conditions for transient turbulent flows in arbitrary geometries," Flow, Turbul. Combust. Formerly: Appl. Sci. Res. **74**, 67 (2005).
[52]P. Schlatter and R. Örlü, "Assessment of direct numerical simulation data of turbulent boundary layers," J. Fluid Mech. **659**, 116 (2010).
[53]A. Lozano-Durán and J. Jiménez, "Effect of the computational domain on direct simulations of turbulent channels up to $Re_\tau = 4200$," Phys. Fluids **26**, 011702 (2014).
[54]P. Schlatter, R. Örlü, Q. Li, G. Brethouwer, J. H. M. Fransson, A. V. Johansson, P. H. Alfredsson, and D. S. Henningson, "Turbulent boundary layers up to $Re_\theta = 2500$ studied through simulation and experiment," Phys. Fluids **21**, 051702 (2009).
[55]R. J. Adrian, C. D. Meinhart, and C. D. Tomkins, "Vortex organization in the outer region of the turbulent boundary layer," J. Fluid Mech. **422**, 1 (2000).
[56]N. S. Vaghefi and C. K. Madnia, "Local flow topology and velocity gradient invariants in compressible turbulent mixing layer," J. Fluid Mech. **774**, 67 (2015).
[57]Y. Morinishi, T. S. Lund, O. V. Vasilyev, and P. Moin, "Fully conservative higher order finite difference schemes for incompressible flow," J. Comput. Phys. **143**, 90 (1998).
[58]T. Watanabe and K. Nagata, "Mixing model with multi-particle interactions for Lagrangian simulations of turbulent mixing," Phys. Fluids **28**, 085103 (2016).
[59]T. Watanabe and K. Nagata, "Gradients estimation from random points with volumetric tensor in turbulence," J. Comput. Phys. **350**, 518 (2017).
[60]T. Watanabe, J. J. Riley, and K. Nagata, "Turbulent entrainment across turbulent-nonturbulent interfaces in stably stratified mixing layers," Phys. Rev. Fluids **2**, 104803 (2017).
[61]R. A. Antonia, H. Abe, and H. Kawamura, "Analogy between velocity and scalar fields in a turbulent channel flow," J. Fluid Mech. **628**, 241 (2009).
[62]H. Suzuki, K. Nagata, Y. Sakai, T. Hayase, Y. Hasegawa, and T. Ushijima, "An attempt to improve accuracy of higher-order statistics and spectra in direct numerical simulation of incompressible wall turbulence by using the compact schemes for viscous terms," Int. J. Numer. Methods Fluids **73**, 509 (2013).

[63]A. W. Vreman and J. G. M. Kuerten, "Comparison of direct numerical simulation databases of turbulent channel flow at $Re_\tau = 180$," Phys. Fluids **26**, 015102 (2014).
[64]P. He, "A high order finite difference solver for massively parallel simulations of stably stratified turbulent channel flows," Comput. Fluids **127**, 161 (2016).
[65]L. P. Erm and P. N. Joubert, "Low-Reynolds-number turbulent boundary layers," J. Fluid Mech. **230**, 1 (1991).
[66]J. Jiménez, S. Hoyas, M. P. Simens, and Y. Mizuno, "Turbulent boundary layers and channels at moderate Reynolds numbers," J. Fluid Mech. **657**, 335 (2010).
[67]A. J. Smits, N. Matheson, and P. N. Joubert, "Low-Reynolds-number turbulent boundary layers in zero and favorable pressure gradients," J. Ship Res. **27**, 147 (1983).
[68]C. B. da Silva, R. R. Taveira, and G. Borrell, "Characteristics of the turbulent/nonturbulent interface in boundary layers, jets and shear-free turbulence," J. Phys.: Conf. Ser. **506**, 012015 (2014).
[69]J. Westerweel, C. Fukushima, J. M. Pedersen, and J. C. R. Hunt, "Momentum and scalar transport at the turbulent/non-turbulent interface of a jet," J. Fluid Mech. **631**, 199 (2009).
[70]R. R. Taveira and C. B. da Silva, "Kinetic energy budgets near the turbulent/nonturbulent interface in jets," Phys. Fluids **25**, 015114 (2013).
[71]O. Terashima, Y. Sakai, K. Nagata, Y. Ito, K. Onishi, and Y. Shouji, "Simultaneous measurement of velocity and pressure near the turbulent/non-turbulent interface of a planar turbulent jet," Exp. Therm. Fluid Sci. **75**, 137 (2016).
[72]T. Watanabe, C. B. da Silva, and K. Nagata, "Multi-particle dispersion during entrainment in turbulent free-shear flows," J. Fluid Mech. **805**, R1 (2016).
[73]T. Watanabe, R. Jaulino, R. R. Taveira, C. B. da Silva, K. Nagata, and Y. Sakai, "Role of an isolated eddy near the turbulent/non-turbulent interface layer," Phys. Rev. Fluids **2**, 094607 (2017).
[74]P. A. Davidson, *Turbulence: An Introduction for Scientists and Engineers* (Oxford University Press, 2004).
[75]S. B. Pope, *Turbulent Flows* (Cambridge University Press, 2000).